nature catalysis

ARTICLES

https://doi.org/10.1038/s41929-018-0084-7

Steering post-C–C coupling selectivity enables high efficiency electroreduction of carbon dioxide to multi-carbon alcohols

Tao-Tao Zhuang[1,2,7], Zhi-Qin Liang[1,7], Ali Seifitokaldani[1,7], Yi Li[2], Phil De Luna[3], Thomas Burdyny[4], Fanglin Che[1], Fei Meng[5], Yimeng Min[1], Rafael Quintero-Bermudez[1], Cao Thang Dinh[1], Yuanjie Pang[4], Miao Zhong[1], Bo Zhang[1,6], Jun Li[4], Pei-Ning Chen[1], Xue-Li Zheng[1], Hongyan Liang[1], Wen-Na Ge[5], Bang-Jiao Ye[5], David Sinton[4], Shu-Hong Yu[2]* and Edward H. Sargent[1]*

Engineering copper-based catalysts that favour high-value alcohols is desired in view of the energy density, ready transport and established use of these liquid fuels. In the design of catalysts, much progress has been made to target the C–C coupling step; whereas comparatively little effort has been expended to target post-C–C coupling reaction intermediates. Here we report a class of core–shell vacancy engineering catalysts that utilize sulfur atoms in the nanoparticle core and copper vacancies in the shell to achieve efficient electrochemical CO_2 reduction to propanol and ethanol. These catalysts shift selectivity away from the competing ethylene reaction and towards liquid alcohols. We increase the alcohol-to-ethylene ratio more than sixfold compared with bare-copper nanoparticles, highlighting an alternative approach to electroproduce alcohols instead of alkenes. We achieve a C_{2+} alcohol production rate of 126 ± 5 mA cm^{-2} with a selectivity of 32 ± 1% Faradaic efficiency.

The renewable-energy-powered electrocatalytic reduction of carbon dioxide (CO_2) to value-added carbon-based products offers to provide crucial energy storage to address growing energy demand[1–5]. Recent progress in electrocatalytically converting CO_2 has resulted in the production of gaseous carbon products such as carbon monoxide[6] (CO), methane[7] (CH_4) and ethylene[8] (C_2H_4) and C_1 liquids such as formate[9–15] (HCOOH).

The production of liquid multi-carbon alcohols is also highly desired, it stands to enable the synthesis of sustainable fuels that leverage high energy densities[16] (21 MJ l^{-1} ethanol, 27 MJ l^{-1} propanol) for long-range and heavy freight transportation applications. Unfortunately, the production of multi-carbon alcohols via direct CO_2 electroreduction remains below that required for economic viability due to the limited selectivity and low activity of present-day catalysts[17,18].

Among electrocatalysts for CO_2 reduction, Cu-based materials are the most prone to reduce CO_2 to products with two or more carbons (C_{2+}), with alkenes traditionally dominating multi-carbon product formation[19–21]. To develop more efficient electrocatalysts for alcohol production, it is crucial to modify the catalyst structure to promote the desired alcohol and suppress alkene electrosynthesis. Additionally, it is vital to understand the mechanisms that underlie selectivity to enable further catalyst refinement.

We reasoned that—because ethylene and ethanol share a penultimate reaction intermediate[22]: *C_2H_3O—we could potentially modify a catalyst's surface structure to target the hydrogenation of this intermediate and thereby promote C_2 liquid production. Suppressing oft-produced ethylene would enhance production and selectivity towards alcohols.

Several avenues have previously been employed to engineer Cu surfaces to tune the energetics of intermediate binding[20,23–26]. Introducing metal atomic vacancy defects influences electrocatalytic performance by adjusting the electronic structure of neighbouring atoms and consequently the energy barriers of the rate-limiting reaction intermediates[27]. Copper sulfide structures are of interest because they can provide a means to form stable surface defects and control the density of surface vacancies[28,29]. Additionally, copper sulfide-derived catalysts merit investigation in view of the long-range modification of the local density of surface states by introducing sulfur into the Cu structure and the effect on CO binding[30].

In this study, we obtained preliminary results that reveal that varying a Cu catalyst by introducing S could lead to a notable difference in the ratio of ethanol to ethylene produced (Supplementary Table 1). These data motivated us to examine a key rate-limiting step along the CO_2-to-C_2 pathway using computational analysis. In the computational studies, we found that a modified Cu_2S core with Cu surface vacancies could account for a modulation in branching in favour of ethanol relative to ethylene. Specifically, density functional theory (DFT) studies examined the energetics seen by the adsorbed CH_2CHO intermediate that might influence alcohol versus ethylene electrosynthesis. These studies point to strategies to switch CO_2 reduction reaction

[1]Department of Electrical and Computer Engineering, University of Toronto, Toronto, Ontario, Canada. [2]Division of Nanomaterials & Chemistry, Hefei National Laboratory for Physical Sciences at Microscale, Collaborative Innovation Center of Suzhou Nano Science and Technology, CAS Center for Excellence in Nanoscience, Department of Chemistry, University of Science and Technology of China, Hefei, Anhui, China. [3]Department of Materials Science and Engineering, University of Toronto, Toronto, Ontario, Canada. [4]Department of Mechanical and Industrial Engineering, University of Toronto, Toronto, Ontario, Canada. [5]State Key Laboratory of Particle Detection and Electronics, University of Science and Technology of China, Hefei, Anhui, China. [6]State Key Laboratory of Molecular Engineering of Polymers, Department of Macromolecular Science, Fudan University, Shanghai, China. [7]These authors contributed equally: Tao-Tao Zhuang, Zhi-Qin Liang, Ali Seifitokaldani. *e-mail: shyu@ustc.edu.cn; ted.sargent@utoronto.ca

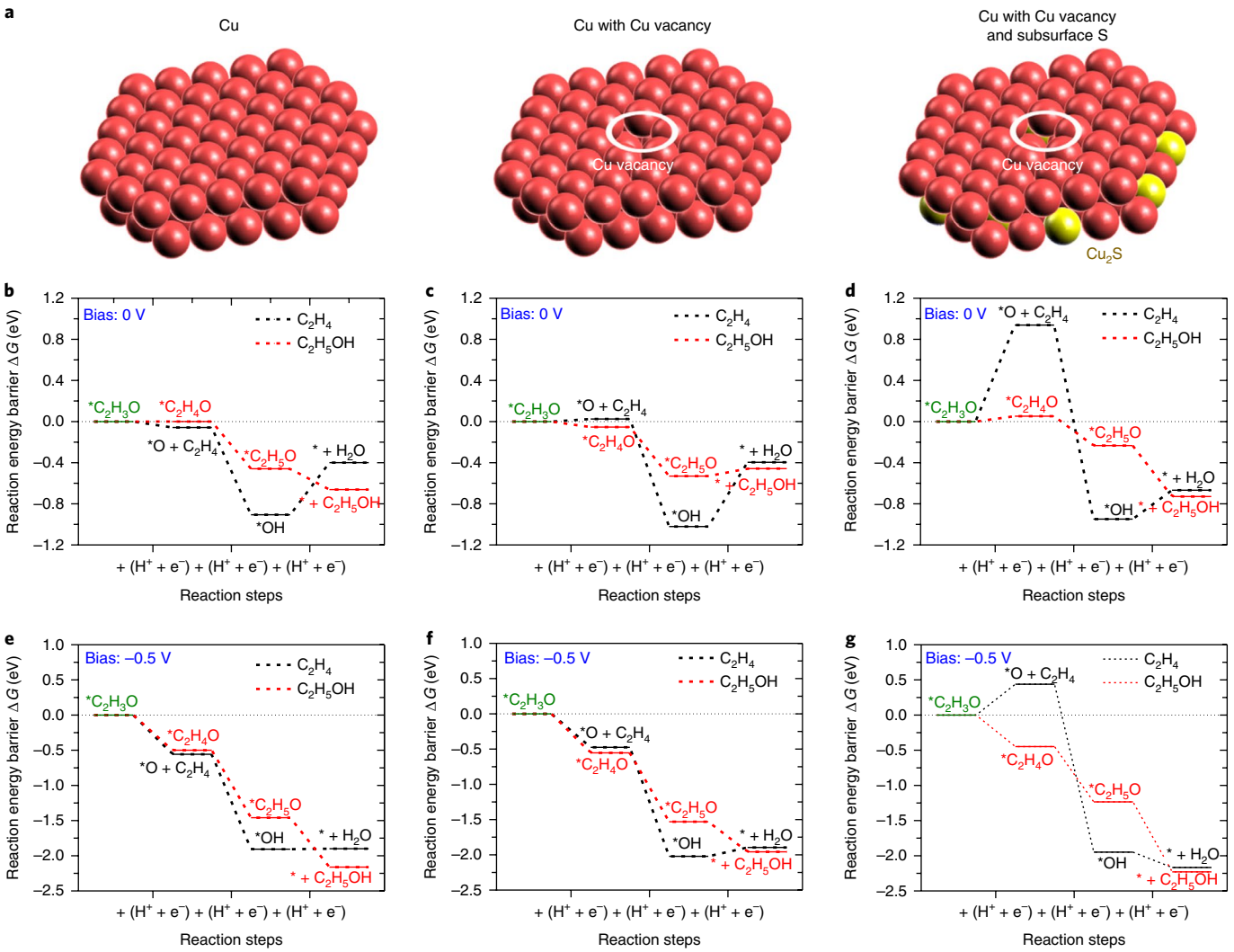

Fig. 1 | Reaction Gibbs free energy diagram. a, Atomic models. **b**–**d**, Reaction Gibbs free energy diagram from the adsorbed C_2H_3O intermediate to ethylene (black lines) and ethanol (red lines) for pristine copper (**b**), Cu with Cu vacancy (**c**) and Cu with Cu vacancy and subsurface S (**d**) slab models. **e**–**g**, The same reaction free energy diagrams after applying a −0.5 V bias potential.

pathways from ethylene to alcohol. We then embarked upon a systematic study of S-enriched Cu and surface vacancies, synthesizing a Cu_2S–Cu-V (where V denotes vacancy) nanoparticle structure that enables the controllable introduction of vacancies on a copper surface shell with a copper sulfide core. Our core–shell-vacancy engineering (CSVE) catalyst enabled us to modify the C_2 reaction pathway, shifting selectivity away from ethylene and towards multi-carbon alcohols.

Results

Theoretical simulations predict selectivity control. To investigate the influence of a modified Cu core–shell structure and surface Cu vacancies on the final ethylene and ethanol reaction steps, we used DFT to characterize changes in energy barriers relative to the case of pristine Cu. Reduction of CO_2 to multi-carbon products proceeds through the dimerization or protonation of adsorbed CO intermediates[31–33]. It has been shown that CO electroreduction to ethanol shares a similar pathway with ethylene until the final three proton-coupled electron transfer steps. At this late stage, the adsorbed CH_2CHO intermediate ($*C_2H_3O$) may proceed to ethanol through further carbon protonation; or to ethylene by leaving an oxygen atom adsorbed on the surface[22,34].

We focused therefore on the effect of surface modifications on the thermodynamics of the adsorbed CH_2CHO intermediate, and in turn on the selectivity for ethylene versus ethanol production. We began by creating three model systems: a pristine copper slab, a copper slab with a single atomic vacancy and a Cu_2S–Cu core–shell model with an atomic vacancy (Fig. 1a, Supplementary Fig. 1). We then explored the following proposed reaction mechanisms representative of ethylene and ethanol production:

Ethylene pathway:

$$*C_2H_3O + (H^+ + e^-) \rightarrow * O + C_2H_4 \quad (1)$$

$$*O + (H^+ + e^-) \rightarrow * OH \quad (2)$$

$$*OH + (H^+ + e^-) \rightarrow * + H_2O \quad (3)$$

Ethanol pathway:

$$*C_2H_3O + (H^+ + e^-) \rightarrow * C_2H_4O \quad (4)$$

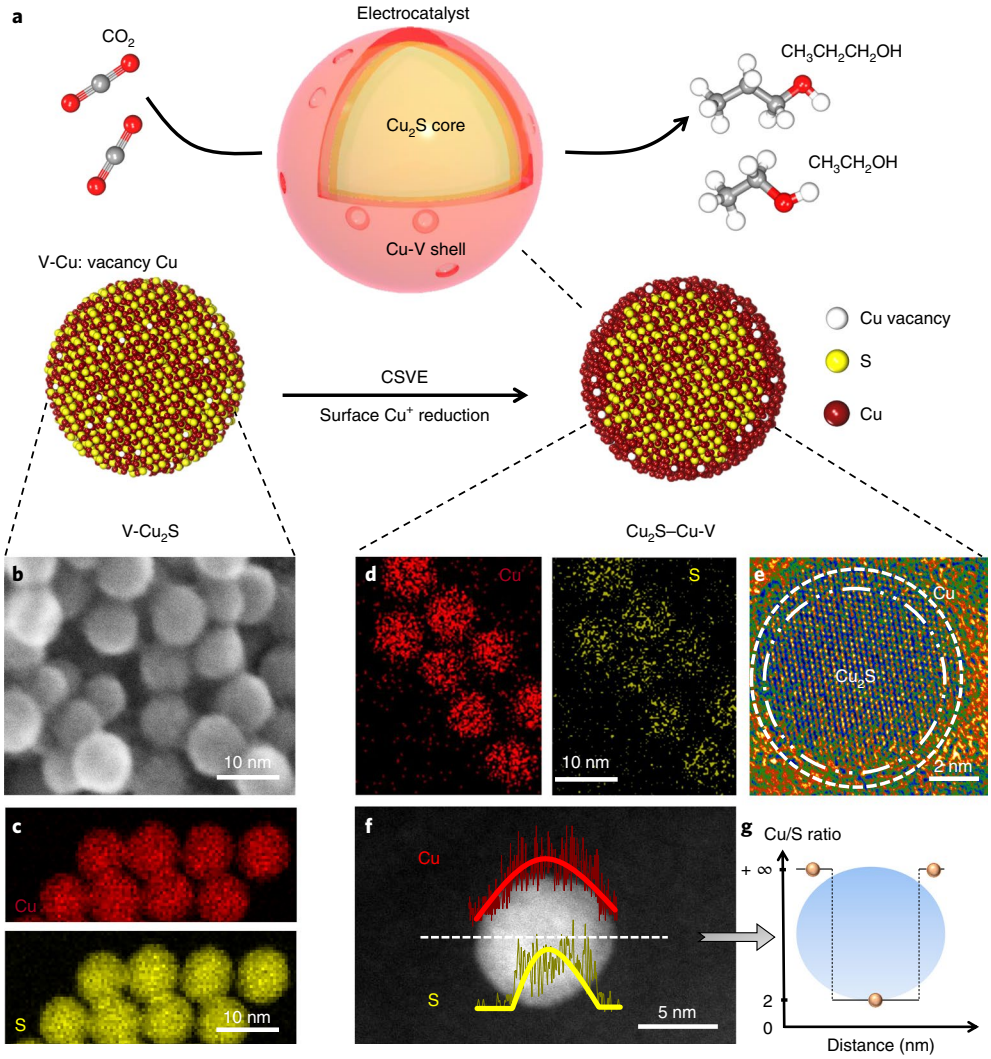

Fig. 2 | Catalyst design and structural characterization. a, Schematic illustration of Cu_2S-Cu-V CSVE electrocatalyst design for production of multi-carbon alcohols from CO_2 reduction. **b**,**c**, TEM (**b**) and EDS (**c**) mapping of the original V-Cu_2S nanoparticles, showing the uniform size and the homogeneous distribution of Cu and S. **d**–**g**, EDS mapping (**d**), high-resolution TEM (**e**), EDS line scan (**f**) and the ratio of Cu/S concentration (**g**) of the reduced CSVE nanocatalysts after electrochemical reduction, showing the removal of S from the nanoparticle surface. V-Cu indicates Cu with surface vacancies.

$$^{*}C_2H_4O + (H^+ + e^-) \rightarrow {}^{*}C_2H_5O \quad (5)$$

$$^{*}C_2H_5O + (H^+ + e^-) \rightarrow {}^{*} + C_2H_5OH \quad (6)$$

We then limited our thermodynamic analyses to mechanistic steps starting with the bound $*CH_2CHO$ intermediate. We found that on pristine copper (Fig. 1b, Supplementary Figs. 2,3 and Supplementary Table 5), both ethylene and ethanol have a low thermodynamic energy barrier (~0 eV) with respective kinetic energy barriers of 0.560 and 0.645 eV (at −0.5 V applied potential, the requirement to overcome the rate–determining C–C coupling step). The introduction of a surface copper vacancy (Fig. 1c, Supplementary Fig. 4 and Supplementary Table 5) slightly increases the energy barrier for ethylene production (0.025 eV), though it remains thermodynamically favoured; whereas the vacancy has a negligible effect on the ethanol pathway. Thus, the activation energy barriers at an applied potential of −0.5 V for both ethylene (0.375 eV) and ethanol (0.531 eV) could be surmounted at room temperature.

Interestingly, a vacancy present on a copper shell with a Cu_2S core increases the energy barrier in the ethylene pathway (1.148 eV), while leaving the ethanol pathway mostly unaffected (0.427 eV) (Fig. 1d). Thus, if one applies an overpotential of 0.5 V (the required overpotential to overcome the early C–C coupling energy barrier), the ethanol pathway remains exergonic, but the ethylene pathway becomes unfavourable (Fig. 1e–g Supplementary Fig. 5 and Supplementary Table 5) suggesting selective production in favour of ethanol is achievable.

These results suggest that subsurface sulfur atoms and copper vacancy defects together shift the balance in favour of ethanol by suppressing ethylene production through this common pathway (details in Supplementary Figs. 1–6 and Supplementary Tables 2–5).

Catalyst synthesis and characterization. In light of these DFT findings, we sought to synthesize a surface-vacancy-enriched copper sulfide–copper core–shell catalyst. We first prepared colloidal vacancy-enriched Cu_2S (V-Cu_2S) nanoparticles. Cuprous sulfide nanoparticles synthesized using the solvothermal method enable controlled copper vacancies in the surface structure of the catalyst[35]. Next, we reduced the V-Cu_2S in a CO_2 saturated electrolyte, yielding

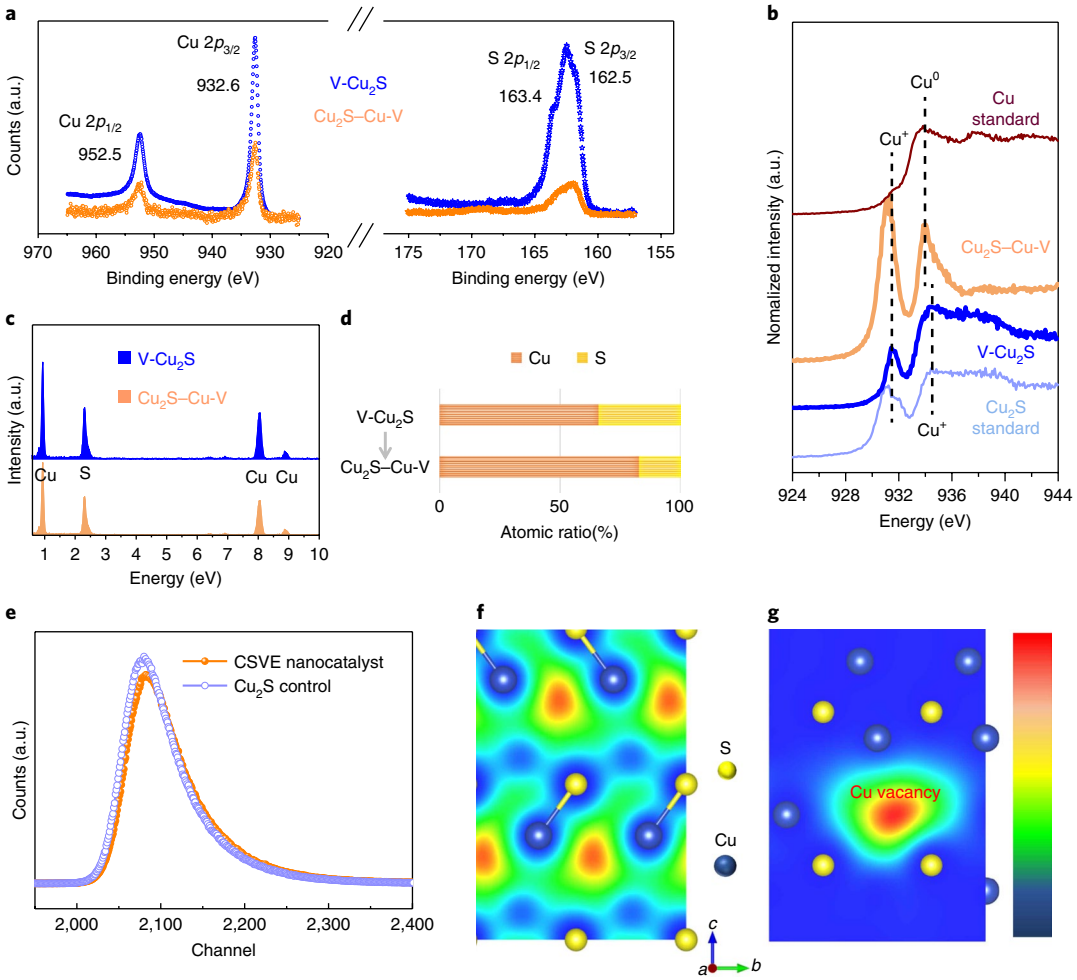

Fig. 3 | Characterization of the CSVE catalyst. a, XPS of the original V-Cu_2S nanoparticles and XPS sputter depth profiling of the derived CSVE catalyst (Cu_2S-Cu-V). **b**, Cu L_3-edge XAS of the original V-Cu_2S nanoparticles, the derived CSVE catalyst, a reference Cu_2S standard and a reference Cu standard. **c**, EDX showing the change in elemental composition between V-Cu_2S and the CSVE catalyst. **d**, The atomic ratio of copper and sulfur in the V-Cu_2S and CSVE catalyst, calculated by XRF. **e**–**g**, Positron lifetime spectra (**e**), simulated result of the positron density distribution in the pure Cu_2S bulk (**f**) and schematic representation of trapped positrons of copper vacancies in the CSVE catayst (**g**).

a reduced metallic copper shell with enriched vacancies surrounding a Cu_2S core (Fig. 2a).

To investigate the core–shell structure and to query the extent of surface vacancies, we analysed the nanoparticles before and after reduction. The morphology of the copper sulfide nanoparticles was characterized using transmission electron microscopy (TEM, Supplementary Fig. 7a), high-resolution TEM (HRTEM, Supplementary Fig. 7b) and high-angle annular dark-field scanning TEM (HAADF-STEM, Fig. 2b and Supplementary Fig. 7c). The nanoparticles have a high degree of uniformity and an average diameter of 8.5 nm. Energy dispersive X-ray spectroscopy (EDS) mapping data (Fig. 2c) reveal that copper and sulfur are distributed evenly throughout the particle. Powder X-ray diffraction (PXRD) analysis (Supplementary Fig. 7d) shows good agreement with the standard $Cu_{1.94}S$ djurleite phase[35,36], thus indicating a non-stoichiometric ratio between copper and sulfur.

The active nanocatalyst used for CO_2 reduction was then produced by electrochemical reduction of the V-Cu_2S nanoparticles, which removed sulfur from the surface, thereby constructing Cu_2S–Cu-V: a Cu_2S core with an ultrathin metallic copper shell containing copper vacancies. In these nanoparticles, elemental Cu enriches the nanostructure, while the sulfur signal is decreased but still present, indicating that a fraction of sulfur has been removed during CO_2 reduction (Fig. 2d–e). To examine the sulfur distribution in the derived structure in detail, we acquired an EDS line scan: it revealed that sulfur mainly concentrates in the core of the nanoparticle, confirming the picture of a Cu_2S–Cu core–shell nanostructure (Fig. 2f–g).

To explore the variation in nanoparticle structure during CO_2 reduction, and gain insight into the electronic configuration, we used X-ray photoelectron spectroscopy (XPS) to probe the chemical composition of the copper sulfide nanoparticles before and after the CO_2 reduction reaction. As shown in Fig. 3a and Supplementary Fig. 8, the Cu peaks, which possess a weak asymmetric tail, agree with a covellite structure[37]. Combining with XPS core level binding energy simulation results (Supplementary Fig. 9), we found further support for the view that the CSVE catalyst possesses Cu defects[37,38]. Results of XPS (Supplementary Fig. 8) and XPS sputter depth profiling (Fig. 3a, orange curve), taken together, show the S 2*p* spectra of the catalyst after reaction. These indicate that sulfur is present at the core of the nanoparticle. Figure 3b shows the Cu L_3-edge soft X-ray absorption spectra (sXAS) of the catalyst and corresponding reference standard materials. The results show that the V-Cu_2S exhibits Cu_2S features before

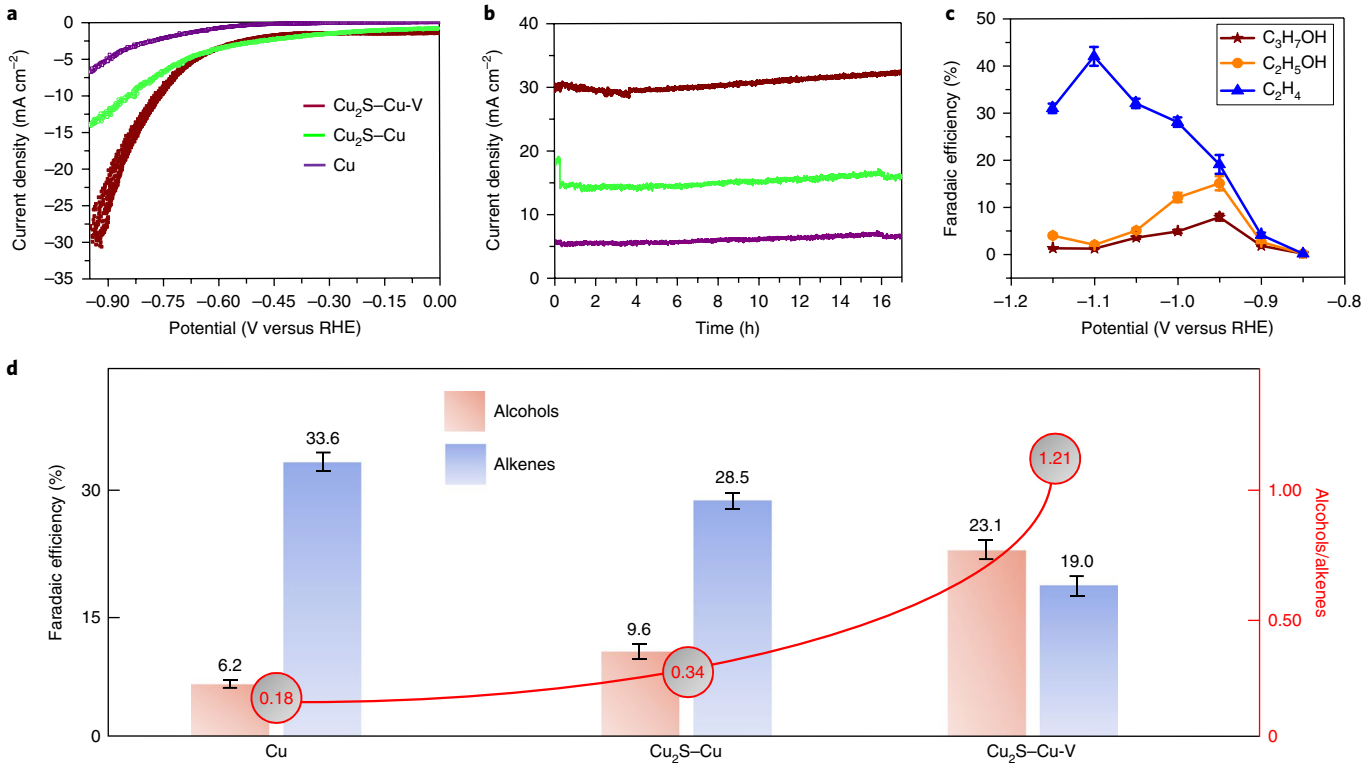

Fig. 4 | CO_2 electrochemical reduction performance in an H-cell system. a, Linear sweep voltammetry curves in a CO_2-saturated 0.1 M $KHCO_3$ aqueous solution for the CSVE and control catalysts. **b**, Chrono-amperometry results at a potential of −0.95 V vesus RHE. **c**, Faradaic efficiencies of alkenes and alcohols on CSVE nanocatalyst at different applied potentials (details in Supplementary Fig. 11). **d**, Faradaic efficiencies of alcohols (ethanol and propanol) and ethylene on different catalysts at the potential of -0.95 V versus RHE (details in Supplementary Table 7). Numbers in red circles show the corresponding Faradaic efficiency ratio of alcohols to alkenes. Error bars correspond to the average taken over at least three measurements.

reaction and both Cu^0 and Cu^+ features after reaction (derived Cu_2S–Cu-V)[39,40]. By simulating the extended X-ray absorption fine structure (EXAFS) fitting of Cu K-edge in reduced space (Supplementary Fig. 10), we found that the Cu–Cu bond distance of the CSVE catalyst becomes larger compared to the case of pure copper. Energy dispersive X-ray spectroscopy (EDX) results show that the sulfur concentration decreased after CO_2 reduction reaction for 16 hours (Fig. 3c). The atomic ratios of Cu/S in the catalyst before (Cu/S = 1.94 ± 0.01) and after (Cu/S = 4.81 ± 0.02) reaction were obtained using X-ray fluorescence (XRF, Fig. 3d).

Positron annihilation spectroscopy (PAS), which probes the type and relative concentration of defect vacancies[41], was carried out to investigate the copper surface. The positron lifetime spectra (Fig. 3e) and the lifetime parameters (Supplementary Table 6) show that both the CSVE catalyst and also the Cu_2S bulk control, exhibit three lifetimes. We assign the shortest lifetime τ_1 (around 260 ps) to the bulk, and the longest component ($\tau_3 > 2$ ns) to the annihilation of orthopositronium atoms formed in the large voids present in the material[42,43]. We ascribe the component τ_2 (approx. 380 ps) to positron annihilation in trapped Cu vacancies. The relative intensities (I) of these lifetimes reflect that copper vacancies and bulk character are predominant in the CSVE nanoparticles and bulk Cu_2S, respectively. Simulated results in Fig. 3f,g reveal the projection of the positron density distribution for the pure Cu_2S bulk and the CSVE nanoparticle sample, indicating the high vacancy-associated concentration in the latter.

Performance in electrochemical CO_2 reduction. To probe electrocatalytic properties, we first characterized the electrochemical CO_2 reduction activity and selectivity using a three-electrode H-cell system. The catalysts were loaded onto a glassy carbon electrode. Linear sweep voltammetry curves were obtained in a CO_2-saturated 0.1 M $KHCO_3$ aqueous solution (Fig. 4a). The CSVE catalyst exhibits a total geometric current density of ~32 mA cm^{-2} at −0.95 V versus a reversible hydrogen electrode (RHE) during 16 h of continuous electrocatalysis (Fig. 4b).

Electrocatalysis was performed using cathodic potentials in the range of −0.85 V to −1.15 V versus RHE (Fig. 4c). As the applied potential becomes more negative (−0.9 V versus RHE), multi-carbon products were observed, indicating that C–C coupling occurs beyond this potential (Supplementary Fig. 11a).

At potentials of −0.95 V vs RHE, 500 mV above the potential at which C–C coupling is first observed, the CSVE nanocatalyst shows peak alcohol production. Interestingly, propanol (C_3H_7OH) and ethanol (C_2H_5OH) follow a similar selectivity trend with changes to the applied potential, indicating that ethanol and propanol share common intermediates along their reaction pathways. This is consistent with the assumption made in our DFT study, wherein we used ethanol as a proxy for overall alcohol electrosynthesis. The maximum Faradaic efficiency for C_3H_7OH and C_2H_5OH reaches 8 ± 0.7% and 15 ± 1% with a partial current density of 2.5 ± 0.1 and 4.8 ± 0.1 mA cm^{-2} at −0.95 V versus RHE, respectively (Fig. 4d and Supplementary Figs. 11,12).

These represent 6, 19, 46 and 44-fold improvements in partial current density for C_{2+} alcohols compared with those of Cu_2S nanoparticles without vacancies, pure Cu nanoparticles, bulk Cu_2S and bulk Cu under the same operating conditions (Supplementary Figs. 13–15).

Moreover, the alcohol-to-ethylene ratio is enhanced from 0.18 on the bare Cu nanoparticles to 1.2, a sixfold increase with the

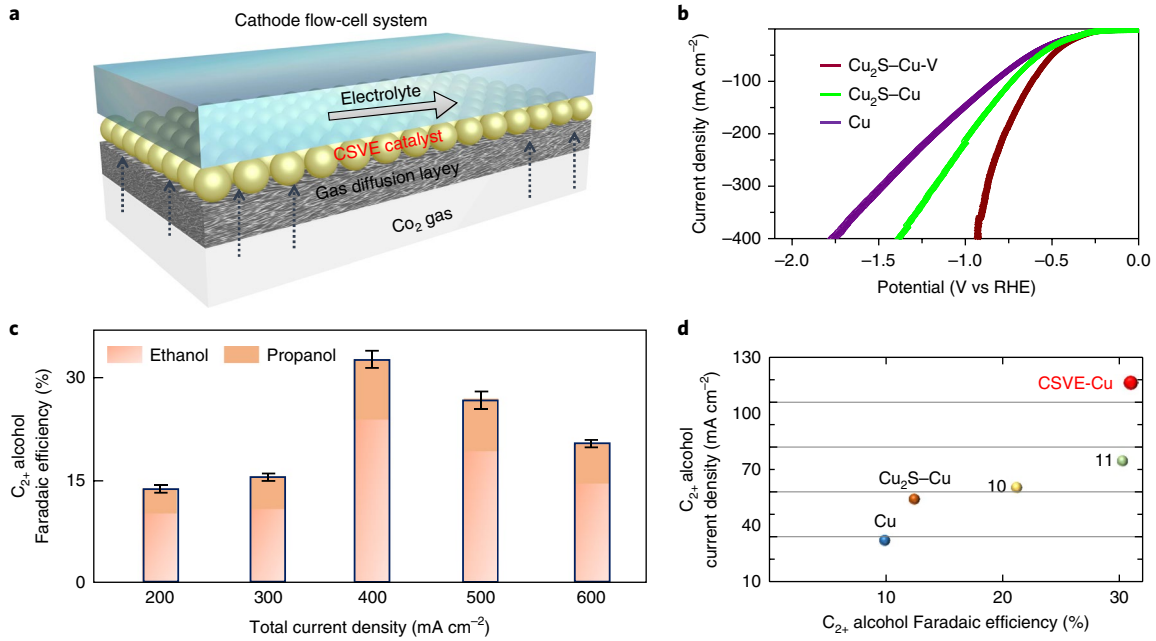

Fig. 5 | CO_2 electrochemical reduction performance in a flow-cell system. a, Schematic illustration of the cathode flow-cell system using a gas-diffusion electrode for CO_2. **b**, Linear sweep voltammetry curves in the 1 M KOH electrolyte for the CSVE and control catalysts. **c**, Faradaic efficiencies of C_{2+} alcohols (ethanol and propanol) on CSVE nanocatalyst in the current density range 200–600 mA cm^{-2} (details in Supplementary Table 10). **d**, Plot of C_{2+} alcohol partial current density versus maximum C_{2+} alcohol Faradaic efficiency for catalysts in a flow-cell system (compared with those from refs [10,11] and details in Supplementary Table 11). Error bars correspond to the average taken over at least three measurements.

CSVE catalyst, while overall C_{2+} selectivity remains similar (Fig. 4d and Supplementary Table 7). It indicates that the Faradaic current was shifted from producing ethylene to producing alcohols. The performance improvement elucidates the synergetic effect of the Cu_2S core and the surface copper vacancies in promoting alcohol production. We should note that it is experimentally challenging to completely decouple the role of copper vacancies and the role of the core sulfur.

To characterize the intrinsic catalytic activity, we measured the electrochemically active surface area of each catalyst. Although the Cu_2S–Cu-V nanoparticles had a slightly larger electrochemically active surface area than the Cu_2S and Cu control nanoparticles, the electrochemically active surface area difference between the CSVE and control catalysts is less than 4% (Supplementary Figs. 16,17 and Supplementary Tables 8,9). The shift in the C_2 production pathway and the high current density towards alcohols is therefore ascribed to the catalyst itself rather than to any substantive increase in electrochemically active surface area.

We then sought a way to engineer the reaction environment to work in tandem with the CSVE catalyst to suppress ethylene and boost multi-carbon alcohol production. At a high pH, the concentration of OH^- will be increased proximate to the catalyst surface affecting the bound O* intermediate along the ethylene pathway (equation (2)), but is expected to leave the ethanol pathway largely unaffected. We turned to a flow-cell configuration that allowed us to operate in alkaline KOH electrolyte without compromising CO_2 availability. We chose highly alkaline KOH as the electrolyte to increase the pH and electrolyte conductivity, and further enhance CO_2 reduction reaction kinetics by suppressing hydrogen evolution[44–46]. The configuration bypasses the low CO_2 solubility in KOH via the diffusion of CO_2 across a gas–liquid interface adjacent to the catalyst surface (Fig. 5a)[47]. We first deposited the catalyst by spray-coating a nanoparticle ink onto a carbon gas-diffusion electrode (details in Supplementary Methods). Linear sweep voltammetry curves (Fig. 5b) of the three catalysts show the lower overpotentials of the CSVE-Cu catalyst at fixed current densities highlighting the improved activity.

We then evaluated the CO_2 reduction reaction activity in the current density range 200–600 mA cm^{-2} in 1 M KOH (Fig. 5c, Supplementary Fig. 18 and Supplementary Table 10), a range enabled by the use of a flow cell and the alkaline electrolyte. For the CSVE-Cu catalyst, we achieved a Faradaic efficiency of 32% for multi-carbon alcohols (C_2H_5OH 25 ± 1% and C_3H_7OH 7 ± 0.5%). The partial current density exceeded 120 mA cm^{-2} for multi-carbon alcohols.

The Faradaic efficiency and partial current density exceeded, by a factor of two, those of control catalysts, including both Cu_2S without vacancy, and also pure Cu (Supplementary Fig. 19). The C_{2+} alcohol partial current density versus maximum C_{2+} alcohol Faradaic efficiency for a range of catalysts reported in the literature is provided in Fig. 5d, Supplementary Fig. 20 and Supplementary Table 11.

Conclusions

By incorporating sulfur atoms in the catalyst core, and copper vacancies in its shell, we realized Cu_2S–Cu-V core–shell nanoparticles that enhance CO_2 reduction to multi-carbon alcohols. DFT calculations suggested the Cu_2S–Cu-V structure steers products beyond alkenes and towards alcohols. Structural characterization, X-ray studies and electrochemical measurements attest to the role of CSVE in improving catalytic performance. These findings indicate an alternative catalytic approach that targets the suppression of unwanted C_2, rather than just C_1, products. This works offers avenues to the design of efficient catalysts that selectively produce higher-carbon liquid alcohols.

Methods

Computational details. The projected augmented wave approach[48,49] and the generalized gradient approximation of Perdew, Burke and Ernzerhof[50] with the DFT-D3 method for van der Waals correction[51] employed in the Vienna ab initio Simulation Package[52] were used to perform all the plane wave DFT computations.

V-Cu_2S nanoparticle synthesis. Synthesis of the copper(I) sulfide nanocrystals with controlled copper vacancies was performed according to a slightly modified version of a previously reported method[35]. In a typical procedure, 130 mg Cu(acetylacetone)$_2$ was dissolved by 30 ml dodecanethiol in a three-neck flask with magnetic stirring under the protection of nitrogen gas and heated at 240 °C for 20 min. The resulting V-Cu_2S nanoparticles were collected by centrifugation, washed with acetone and hexane three times and dried within a vacuum chamber.

Cu_2S nanoparticle synthesis. The copper(I) sulfide nanoparticles without copper vacancies were prepared using a previously reported method[53]. 1.25 mmol of ammonium diethyldithiocarbamate was mixed with 10 ml of dodecanethiol and 17 ml of oleic acid in a three-neck flask. The solution was heated up to 110 °C under argon flow followed by a quick injection of a suspension of 1 mmol copper(II) acetylacetonate and 3 ml oleic acid. The solution was then quickly heated up to 180 °C and kept at that temperature for 20 min. The resulting Cu_2S nanoparticles were collected by centrifugation, washed with acetone and hexane three times and further dried in a vacuum chamber.

Cu nanoparticle synthesis. In a typical synthesis of metallic copper nanoparticles[54], 1.2 mmol CuBr and 15 ml oleylamine were mixed in a three-neck flask under stirring at 80 °C for 30 min under nitrogen protection, then 1 mmol trioctylphosphine was added and reacted at 80 °C until a colourless solution was obtained. The mixed solution was heated to 260 °C quickly and kept for 1 h. The resulting Cu nanoparticles were precipitated by centrifugation, purified with acetone and hexane three times and further dried in a vacuum chamber.

Electrochemical measurements. Electrocatalytic measurements were carried out in a three-electrode system at an electrochemical station (AUT50517). All potentials were measured against an Ag/AgCl reference electrode (3 M KCl, BASi) and converted to the RHE reference scale using:

$$E\ (\text{vs RHE}) = E\ (\text{vs Ag/AgCl}) + 0.197\ V + 0.0591 \times \text{pH}$$

where E represents the potential, and V reprensents volt, the unit of the potential.

CO_2 reduction electrolysis and product analysis. Electrolysis was performed in a two-compartment electrochemical H-cell with a proton exchange membrane (Nafion 117) as the separator and a flow-cell configuration consisting of a gas-diffusion layer with an anion exchange membrane.

Additional details. Sample characterizations as well as the electrochemical measurements and computational simulation details are provided in the Supplementary Information.

Data availability. The data that support the plots within this paper and other findings of this study are available from the corresponding author upon reasonable request.

Received: 8 September 2017; Accepted: 26 April 2018;
Published online: 11 June 2018

References

1. Gao, S. et al. Partially oxidized atomic cobalt layers for carbon dioxide electroreduction to liquid fuel. *Nature* **529**, 68–71 (2016).
2. Asadi, M. et al. Nanostructured transition metal dichalcogenide electrocatalysts for CO_2 reduction in ionic liquid. *Science* **353**, 467–470 (2016).
3. Liu, M. et al. Enhanced electrocatalytic CO_2 reduction via field-induced reagent concentration. *Nature* **537**, 382–386 (2016).
4. Lin, S. et al. Covalent organic frameworks comprising cobalt porphyrins for catalytic CO_2 reduction in water. *Science* **349**, 1208–1213 (2015).
5. Seh, Z. W. et al. Combining theory and experiment in electrocatalysis: insights into materials design. *Science* **355**, eaad4998 (2017).
6. Rogers, C. et al. Synergistic enhancement of electrocatalytic CO_2 reduction with gold nanoparticles embedded in functional graphene nanoribbon composite electrodes. *J. Am. Chem. Soc.* **139**, 4052–4061 (2017).
7. Li, Y. et al. Structure-sensitive CO_2 electroreduction to hydrocarbons on ultrathin 5-fold twinned copper nanowires. *Nano Lett.* **17**, 1312–1317 (2017).
8. Mistry, H. et al. Highly selective plasma-activated copper catalysts for carbon dioxide reduction to ethylene. *Nat. Commun.* **7**, 12123 (2016).
9. Saberi Safaei, T. et al. High-density nanosharp microstructures enable efficient CO_2 electroreduction. *Nano Lett.* **16**, 7224–7228 (2016).
10. Lei, F. et al. Metallic tin quantum sheets confined in graphene toward high-efficiency carbon dioxide electroreduction. *Nat. Commun.* **7**, 12697 (2016).
11. Klinkova, A. et al. Rational design of efficient palladium catalysts for electroreduction of carbon dioxide to formate. *ACS Catal.* **6**, 8115–8120 (2016).
12. ZHU, Q.-G. et al. Cu_2S on Cu foam as highly efficient electrocatalyst for reduction of CO_2 to formic acid. *Acta Phys. Chim. Sin.* **32**, 261–266 (2016).
13. Zhu, Q. et al. Efficient reduction of CO_2 into formic acid on a lead or tin electrode using an ionic liquid catholyte mixture. *Angew. Chem. Int. Ed.* **55**, 9012–9016 (2016).
14. Shinagawa, T., Larrazábal, G. O., Martín, A. J., Krumeich, F. & Perez-Ramirez, J. Sulfur-modified copper catalysts for the electrochemical reduction of carbon dioxide to formate. *ACS Catal.* **8**, 837–844 (2017).
15. Huang, Y., Deng, Y., Handoko, A. D., Goh, G. K. & Yeo, B. S. Rational design of sulfur-doped copper catalysts for the selective electroreduction of carbon dioxide to formate. *ChemSusChem* **11**, 320–326 (2018).
16. Schouten, K. J. P., Calle-Vallejo, F. & Koper, M. A step closer to the electrochemical production of liquid fuels. *Angew. Chem. Int. Ed.* **53**, 10858–10860 (2014).
17. Li, C. W. & Kanan, M. W. CO_2 reduction at low overpotential on Cu electrodes resulting from the reduction of thick Cu_2O films. *J. Am. Chem. Soc.* **134**, 7231–7234 (2012).
18. Loiudice, A. et al. Tailoring copper nanocrystals towards C_2 products in electrochemical CO_2 reduction. *Angew. Chem. Int. Ed.* **55**, 5789–5792 (2016).
19. Gawande, M. B. et al. Cu and Cu-based nanoparticles: synthesis and applications in catalysis. *Chem. Rev.* **116**, 3722–3811 (2016).
20. Hahn, C. et al. Engineering Cu surfaces for the electrocatalytic conversion of CO_2: controlling selectivity toward oxygenates and hydrocarbons. *Proc. Natl Acad. Sci. USA* **114**, 5918–5923 (2017).
21. De Luna, P. et al. Catalyst electro-redeposition controls morphology and oxidation state for selective carbon dioxide reduction. *Nat. Catal.* **1**, 103–110 (2018).
22. Kortlever, R., Shen, J., Schouten, K. J. P., Calle-Vallejo, F. & Koper, M. T. Catalysts and reaction pathways for the electrochemical reduction of carbon dioxide. *J. Phy. Chem. Lett.* **6**, 4073–4082 (2015).
23. Adit Maark, T. & Nanda, B. R. K. Enhancing CO_2 electroreduction by tailoring strain and ligand effects in bimetallic copper–rhodium and copper–nickel heterostructures. *J. Phy. Chem. C* **121**, 4496–4504 (2017).
24. van den Berg, R. et al. Structure sensitivity of Cu and CuZn catalysts relevant to industrial methanol synthesis. *Nat. Commun.* **7**, 13057 (2016).
25. Xiao, H., Goddard, W. A., Cheng, T., & Liu, Y. Cu metal embedded in oxidized matrix catalyst to promote CO_2 activation and CO dimerization for electrochemical reduction of CO_2. *Proc. Natl Acad. Sci. USA* **114**, 6685–6688 (2017).
26. Favaro, M. et al. Subsurface oxide plays a critical role in CO2 activation by Cu(111) surfaces to form chemisorbed CO2, the first step in reduction of CO2. *Proc. Natl Acad. Sci. USA* **114**, 6706–6711 (2017).
27. Kasatkin, I., Kurr, P., Kniep, B., Trunschke, A. & Schlögl, R. Role of lattice strain and defects in copper particles on the activity of Cu/ZnO/Al_2O_3 catalysts for methanol synthesis. *Angew. Chem. Int. Ed.* **46**, 7324–7327 (2007).
28. Liu, X. et al. Size-controlled synthesis of $Cu_{2-x}E$ (E = S, Se) nanocrystals with strong tunable near-infrared localized surface plasmon resonance and high conductivity in thin films. *Adv. Funct. Mater.* **23**, 1256–1264 (2013).
29. Luther, J. M., Jain, P. K., Ewers, T. & Alivisatos, A. P. Localized surface plasmon resonances arising from free carriers in doped quantum dots. *Nat. Mater.* **10**, 361–366 (2011).
30. Hu, X. & Hirschmugl, C. Long-range metal-mediated interactions between S and CO on Cu(100). *Phys. Rev. B* **72**, 205439 (2005).
31. Montoya, J. H., Shi, C., Chan, K. & Nørskov, J. K. Theoretical insights into a CO dimerization mechanism in CO_2 electroreduction. *J. Phy. Chem. Lett.* **6**, 2032–2037 (2015).
32. Montoya, J. H., Peterson, A. A. & Nørskov, J. K. Insights into C–C coupling in CO_2 electroreduction on copper electrodes. *ChemCatChem* **5**, 737–742 (2013).
33. Schouten, K. J. P., Kwon, Y., van der Ham, C. J. M., Qin, Z. & Koper, M. T. M. A new mechanism for the selectivity to C_1 and C_2 species in the electrochemical reduction of carbon dioxide on copper electrodes. *Chem. Sci.* **2**, 1902–1909 (2011).
34. Calle-Vallejo, F. & Koper, M. Theoretical considerations on the electroreduction of CO to C_2 species on Cu(100) electrodes. *Angew. Chem. Int. Ed.* **52**, 7282–7285 (2013).
35. Zhuang, T. T., Fan, F. J., Gong, M. & Yu, S. H. $Cu_{1.94}S$ nanocrystal seed mediated solution-phase growth of unique Cu_2S-PbS heteronanostructures. *Chem. Commun.* **48**, 9762–9764 (2012).
36. Han, S. K., Gong, M., Yao, H. B., Wang, Z. M. & Yu, S. H. One-pot controlled synthesis of hexagonal-prismatic $Cu_{1.94}S$-ZnS, $Cu_{1.94}S$-ZnS-$Cu_{1.94}S$, and $Cu_{1.94}S$-ZnS-$Cu_{1.94}S$-ZnS-$Cu_{1.94}S$ heteronanostructures. *Angew. Chem. Int. Ed.* **51**, 6365–6368 (2012).
37. Zhuang, T.-T. et al. Integration of semiconducting sulfides for full-spectrum solar energy absorption and efficient charge separation. *Angew. Chem. Int. Ed.* **55**, 6396–6400 (2016).
38. Xie, Y. et al. Copper sulfide nanocrystals with tunable composition by reduction of covellite nanocrystals with Cu^+ ions. *J. Am. Chem. Soc.* **135**, 17630–17637 (2013).

39. Kvashnina, K. et al. Electronic structure of complex copper systems probed by resonant inelastic X-ray scattering at Cu L_3 edge. *Phys. B* **404**, 3559–3566 (2009).
40. Todd, E., Sherman, D. & Purton, J. Surface oxidation of chalcopyrite ($CuFeS_2$) under ambient atmospheric and aqueous (pH 2–10) conditions: Cu, Fe L- and O K-edge X-ray spectroscopy. *Geochim. Cosmochim. Acta* **67**, 2137–2146 (2003).
41. Chakraverty, S., Mitra, S., Mandal, K., Nambissan, P. & Chattopadhyay, S. Positron annihilation studies of some anomalous features of Ni Fe_2O_4 nanocrystals grown in SiO_2. *Phys. Rev. B* **71**, 024115 (2005).
42. Li, Z. et al. Dual vacancies: an effective strategy realizing synergistic optimization of thermoelectric property in BiCuSeO. *J. Am. Chem. Soc.* **137**, 6587–6593 (2015).
43. Gao, S. et al. Highly efficient and exceptionally durable CO_2 photoreduction to methanol over freestanding defective single-unit-cell bismuth vanadate layers. *J. Am. Chem. Soc.* **139**, 3438–3445 (2017).
44. Ma, S., Luo, R., Moniri, S., Lan, Y. & Kenis, P. J. A. Efficient electrochemical flow system with improved anode for the conversion of CO_2 to CO. *J. Electrochem. Soc.* **161**, F1124–F1131 (2014).
45. Ma, S., Lan, Y., Perez, G. M. J., Moniri, S. & Kenis, P. J. A. Silver supported on titania as an active catalyst for electrochemical carbon dioxide reduction. *ChemSusChem* **7**, 866–874 (2014).
46. Thang Dinh, C. et al. CO_2 electroreduction to ethylene via hydroxide-mediated copper catalysis at an abrupt interface. *Science* **360**, 783–787 (2018).
47. Ma, S. et al. One-step electrosynthesis of ethylene and ethanol from CO_2 in an alkaline electrolyzer. *J. Power Sources* **301**, 219–228 (2016).
48. Blöchl, P. E. Projector augmented-wave method. *Phys. Rev. B* **50**, 17953 (1994).
49. Kresse, G. & Joubert, D. From ultrasoft pseudopotentials to the projector augmented-wave method. *Phys. Rev. B* **59**, 1758 (1999).
50. Perdew, J. P., Burke, K. & Ernzerhof, M. Generalized gradient approximation made simple. *Phys. Rev. Lett.* **77**, 3865 (1996).
51. Muttaqien, F. et al. CO_2 adsorption on the copper surfaces: van der Waals density functional and TPD studies. *J. Phys. Chem. C* **147**, 094702 (2017).
52. Kresse, G. & Furthmüller, J. Efficient iterative schemes for ab initio total-energy calculations using a plane-wave basis set. *Phys. Rev. B* **54**, 11169 (1996).
53. Wu, Y., Wadia, C., Ma, W., Sadtler, B. & Alivisatos, A. P. Synthesis and photovoltaic application of copper (I) sulfide nanocrystals. *Nano Lett.* **8**, 2551–2555 (2008).
54. Guo, H. et al. Shape-selective formation of monodisperse copper nanospheres and nanocubes via disproportionation reaction route and their optical properties. *J. Phys. Chem. C* **118**, 9801–9808 (2014).

Acknowledgements

This work was supported by TOTAL American Services, the Ontario Research Fund Research Excellence programme, the Natural Sciences and Engineering Research Council (NSERC) of Canada, the CIFAR Bio-Inspired Solar Energy programme and a University of Toronto Connaught grant. S.-H.Y. acknowledges funding from the National Natural Science Foundation of China (grant 21431006) and the Foundation for Innovative Research Groups of the National Natural Science Foundation of China (grant 21521001). All DFT computations were performed on the IBM BlueGene/Q supercomputer with support from the Southern Ontario Smart Computing Innovation Platform (SOSCIP). SOSCIP is funded by the Federal Economic Development Agency of Southern Ontario, the Province of Ontario, IBM Canada, Ontario Centres of Excellence, Mitacs and 15 Ontario academic member institutions. Z.L. acknowledges a scholarship from the China Scholarship Council (CSC) (201607090041). A.S. acknowledges Fonds de Recherche du Quebec—Nature et Technologies (FRQNT) for support in the form of a postdoctoral fellowship award. P.D.L. acknowledges NSERC for support in the form of a Canada Graduate Scholarship doctoral award. P.D.L. also wishes to acknowledge Y. Hu and the Canadian Light Source for assistance with X-ray absorption experiments. The authors thank A. Ip, Y. Wang, J. Fan, J. Li, C. Zou and Y. Zhou from the University of Toronto for fruitful discussions.

Author contributions

E.H.S. and S.-H.Y. supervised the project. T.-T.Z. designed and carried out the experiments. Z.-Q.L. helped to investigate the performance measurements. A.S., F.C. and Y.M. carried out simulations. Y.L. helped to characterize the structure of catalyst. P.D.L. and R.Q.-B. performed the X-ray spectroscopy measurements. F.M. and B.-J.Y. carried out positron annihilation. All authors discussed the results and assisted during manuscript preparation.

Competing interests

The authors declare no competing interests.

Additional information

Supplementary information is available for this paper at https://doi.org/10.1038/s41929-018-0084-7.

Reprints and permissions information is available at www.nature.com/reprints.

Correspondence and requests for materials should be addressed to S.-H.Y. or E.H.S.

Publisher's note: Springer Nature remains neutral with regard to jurisdictional claims in published maps and institutional affiliations.